Estimation of plastic deformation capacity for I‐shaped beams with local buckling under compressive and tensile forces

doi: 10.1002/2475-8876.12066

The category

Translated paper[1]

Title

Estimation of Plastic Deformation Capacity for I-shaped Beams with Local Buckling under Compressive and Tensile Forces

Full names of all authors

Yoshihiro Kimura [1], Atsushi Suzuki [2*], and Kazuhiko Kasai [3]

[1] Professor at New Creation Hatchery Center, Tohoku University, 6-6-11-1216, Aoba, Aza, Aramaki, Aoba Ward, Sendai City, Miyagi Prefecture, 980-8579, Japan (E-mail: kimura@m.tohoku.ac.jp, Tel.: +81-(0)22-795-7865, Fax: +81-(0)22-795-7865)

[2] Graduate Student at Graduate School of Engineering, Tohoku University, 6-6-11-1215, Aoba, Aza, Aramaki, Aoba Ward, Sendai City, Miyagi Prefecture, 980-8579, Japan (E-mail: atsushi.suzuki.d5@tohoku.ac.jp, Tel.: +81-(0)90-2791-7316)

[3] Professor at Laboratory for Future Interdisciplinary Research of Science and Technology, Tokyo Institute of Technology, G-5-14, 4259, Nagatsuta Town, Midori Ward, Yokohama City, Kanagawa Prefecture, 226-8503, Japan (E-mail: kasai.k.ac@m.titech.ac.jp, Tel.: +81-(0)45-924-5512, Fax: +81-(0)45-924-5525)

[*] *Corresponding Author*

Atsushi Suzuki, AIJ membership number: 1303948

[1] The Japanese version of this paper was published in Volume 81, Issue 730, Pages 2133-2142, DOI: 10.3130/aijs.81.2133 of Journal of Structural and Construction Engineering (Transactions of AIJ). The authors have obtained permission for secondary publication of the English version in another journal from the Editor of Journal of Structural and Construction Engineering (Transactions of AIJ). This paper is based on the translation of the Japanese version with some slight modifications.

Abstract

During earthquakes, I-shaped beams installed in a braced structure are subjected to a bending moment and compressive and tensile axial forces transmitted from the braces. The buckling behavior of a beam under the impact of an earthquake is thereby more complex than that under no axial force or constant compressive axial forces considered in previous studies. In this paper, cyclic loading tests and numerical analyses are presented with emphasis on cyclic buckling behavior and moment and deformation capacity of the beams subjected to synchronized flexural and axial loading. As a result, it is confirmed that the I-shaped beams originate local buckling under compressive axial force, whereas the strength is regained up to the full plastic bending moment under tensile force. Based on the results obtained, this paper presents evaluation formulae for estimating the ultimate strength, plastic deformation capacity, and cumulative plastic deformation capacity. Finally, an empirical formula to convert cumulative plastic deformation capacity into hysteretic energy dissipation is proposed.

Keywords

I-shaped Beam, Reversed Axial Force, Local Buckling, Equivalent Width-thickness Ratio, Plastic Deformation Capacity, Cumulative Plastic Deformation Capacity

1. Introduction

1.1 Research Background

Dampers have recently been used extensively in Japan for the steel structures to reduce the response and damage of buildings during the earthquakes because: 1) the high-rise buildings often requiring drift control are usually steel structures, 2) installation of dampers on the steel structures is simplest, and 3) evaluation of the amount of damping is relatively straightforward by virtue of the clear elastic hysteresis of the steel frames.

The most widely used damper in Japan is the buckling restrained brace (BRB). When this brace is

installed, the beams in the frame are subjected to axial force as a horizontal component of the damper force during earthquakes, and the magnitude of this force can reach as much as 30% of the beam axial yield strength [1)]. The BRB installed in the steel frame shows a stable spindle-shape hysteresis loop [2)], making the increase in beam axial force more rapid than the increase in the bending moment during sidewise swaying of the frame. Therefore, the stress of beams in a frame with BRB differs from the stress of the usual moment resisting frame, which carries a small axial force to the beams. However, this point is often neglected because the floor is usually assumed to be rigid axially when structural engineers analyze braced frames. Moreover, I-shaped beam sections are often designed to be deeper and narrower to economically enhance the flexural stiffness and strength like those in conventional moment resisting frame, although these beams originate unstable buckling behaviors such as the local buckling and lateral-torsional buckling compared with the H-shaped column sections. The current design guideline, "Recommended Provisions for Seismic Damping Systems Applied to Steel Structures" [3)], therefore requires the use of the section as a column rather than a beam when the axial force in the beam is equal to or greater than 15% of its yield strength. The requirement, however, assumes a constant compressive axial force, in contrast to the transmitted forces from BRBs reversing between compression and tension during the earthquakes, and the buckling behaviors of the beam under such axial forces and cyclic bending moment considerably differs from those forces and bending moments considered in the guideline. This issue, therefore, must be addressed to clarify the performance of beams in the frame installed with BRBs.

In contrast to this need, previous research [4)~12)] has been limited only to the local buckling of I-shaped beams under the cyclically applied bending moment. The proposed the evaluation formulae of plastic deformation capacity and cumulative plastic deformation capacity [4), 11), 12)] consider the width-thickness ratio of plate elements (flange and web) and shear span-to-depth ratio. Recently, Kimura extended the concept of the Bauschinger effect for evaluating the enlargement of hysteretic energy dissipation due to cyclic loading with respect to the enlargement due to equivalent monotonic loading [11)].

However, these studies [11), 12)] do not consider the cases of additional application of axial loading, which can cause early web local buckling and subsequent degradation of the beam.

1.2 Organization

This research evaluates the ultimate strength, plastic deformation capacity, cumulative plastic deformation capacity, and hysteretic energy dissipation of I-shaped beams subjected to cyclic bending deformation and alternating axial forces in braced structures.

Kimura et al. experimentally demonstrated that the moment-rotation curves of the beams after reaching ultimate moment degrade more rapidly under a larger compressive axial force [13)]. This research will predict such behavior, as well as the ultimate strength, plastic deformation capacity, and cumulative plastic deformation capacity, by extending the evaluation formula proposed by Ikarashi and Hasegawa [14)].

However, the tensile axial force case leads to significant hardening behavior due to the pinching of the moment-rotation curve. Considering this, a prediction rule for the hysteretic energy dissipation under alternating compressive and tensile axial forces will be proposed by extending Kimura's formula for the case of no axial forces [11)].

The organization of this paper is as follows. Chapter 2 scrutinizes the local buckling behavior of the beams under reversed axial forces through cyclic loading tests and finite element analyses. Chapter 3 applies the width-thickness ratio proposed in Refs. 11) and 12) to the results of loading tests and numerical analyses, and their applicability is investigated. In addition, the structural performance of I-shaped beams under the reversed axial forces are evaluated based on the width-thickness ratio considering the influence of the axial force in this research. Chapter 4 summarizes the findings obtained in this paper.

2. Buckling Behavior of I-shaped Beams under Alternating Axial Forces

In this chapter, the influence of the magnitude of axial force and difference of beam section on the

ultimate strength, plastic deformation capacity, and cumulative plastic deformation capacity of I-shaped beams under the alternating axial forces are investigated through cyclic loading tests and finite element analyses.

2.1 Outline of Cyclic Loading Tests on I-shaped Beams under Alternating Axial Forces

The experimental set-up is shown in Fig. 1. The specimen is installed between the slide table and the loading frame. Horizontal force is applied by the horizontal jack (1000 kN), and axial force is applied by the vertical jacks installed on the right and left sides of the frame. The out-of-plane displacements of loading frame and slide table are constrained. Fig. 2 shows the concept of the loading test. The displacement of the beam δ_h is measured at the bottom, and the bending moment becomes zero at the center of the frame. The orientation of the axial force of the beam goes to the column-beam joint from the inflection point on the brace frame, in contrast to the columns, which are subjected to the constant axial force going vertically downward. Therefore, the orientation of the axial force deviates from the center of the web with an increment in the bending deformation. This experiment models the cantilever beam subjected to the reversed axial forces from the brace by fixing the orientation of the axial force on the centroid of the web and the jacks on the right and left sides give equal axial force (N_L=N_R). However, the direction of the axial force deviates from the centroid of the beam section, like the beams in the braced frame under a large deformation.

Fig. 3 shows a case of the loading protocol. The loading is conducted as alternating gradual increase loadings (one cycle or two cycles) at one loading amplitude, the same as Ref. 13). The loading amplitude is controlled by a normalized horizontal displacement of δ_h/δ_p=1, 2, 4, or 6 regardless of the magnitude of the axial force, where δ_p is the yield displacement (=$M_p l^2/3EI$) and M_p is the full plastic bending moment. Fig. 4 shows the loading protocol of the axial force. Since the damper deformation prior to yielding is usually small [15)], the damper deformation can be considered to indicate that the difference in the damper stiffness gives little influence on the ultimate strength and plastic deformation capacity. The loading protocol of the axial force is, thereby, determined to be the rigid-plastic hysteresis

to model the ideal damper. Thus, the direction of the axial force switches when the horizontal force is reversed to zero [13]. N_{max} in the vertical axis is a maximum axial force. N_{max} is determined by the axial force ratio, $n(=N_{max}/N_y)$=0, 0.15, 0.3, where N_y is the yield axial strength.

Fig. 5 illustrates the position to attach the strain gauges. The beam length L, the distance from the endplate to the horizontal jack, is 1500 mm. The strain gauges investigate the distribution of out-of-plane deformation and the origination of local buckling.

The list of specimens is tabulated in Table 1. The total number of specimen is 7: 4 of them are from Kimura's experiment [13], and 3 are tested in this research. The specimens from Kimura's experiment [13] are marked by * beside their designations. The parameters are the beam section, the number of the loading cycle at each loading amplitude, and the magnitude of the axial force ratio (n=0, 0.15, 0.3). The designation of the specimen is determined by the following rule: 1) the first letter is the beam section, 2) the second number is the loading cycle at each loading amplitude (1: one cycle, 2: two cycles), 3) the third letter is the loading protocol of the axial force (N: no axial force, R: alternating axial force), and 4) the last number is the magnitude of the axial force ratio, n. The full plastic bending moment, M_p, the yield bending moment, M_y, and the yield axial strength, N_y, are displayed beside the beam section.

The material property is given in Table 2. The type of steel is SS400, and the yield stress varies from 330 to 352N/mm^2.

2.2 Outline of Numerical Analyses on I-shaped Beams under Alternating Axial Forces

In this section, the elasto-plastic large deformation analyses are carried out using Abaqus (version 6.14-5), an FEA software package [16], manufactured by Dassault Systems. Fig. 6 illustrates the numerical model. The numerical model consists of 4-noded shell elements, and the beam-end is defined as a rigid body. The numerical model ranging from z=0 to L_1 (=L/3) is divided into 8 elements in the flange and 16 elements in the web to grasp the buckling behavior accurately. The partition becomes coarse near the free end. The horizontal and axial forces are applied at the top of the numerical model. Imperfections of the flange and web plates are defined based on the deformation of the buckling

eigenvalue analysis, and their maximum magnitudes are standardized as 1% of the flange and web thicknesses, respectively. One side of the beam is a fixed end, and the other side is fixed on the *x*-axis. The loading protocol of the horizontal force and the axial force is the alternating gradual increase in loading (Fig. 3) and alternating axial force (Fig. 4), respectively. The horizontal force is controlled by the normalized horizontal displacement δ_h/δ_p=1, 2, 4, 6, 8, or 10 regardless of the magnitude of the axial force. The axial force reverses when the horizontal force, *P*, is reversed to zero, the same as the cyclic loading test stated in the previous section. Fig. 7 illustrates the way to control the orientation of the axial force. One element is attached to connect the bottom and top of the numerical model and the axial force is applied in parallel to the added element. The element remains elastic, and its stiffness is small so that it can carry a small load.

The list of numerical models is tabulated in Table 3. The analytical parameters possess the different flange width, flange thickness, and web thickness, whereas the beam height and beam length are fixed as *H*=300 mm and *L*=1500 mm, respectively. The normalized flange width-thickness ratio $b/t_f\sqrt{\sigma_{yf}/E}$ is 0.20 to 0.35, and the normalized web width-thickness ratio $d/t_w\sqrt{\sigma_{yw}/E}$ is 1.34 to 2.40. The beams are classified as P-I-1 or P-II as beams and P-I-2 or P-III for columns in "Recommendation for Limit State Design of Steel Structures" [17] published by the Architectural Institute of Japan. The equivalent width-thickness ratio is calculated by the following equation proposed by Kadono et al. [18].

$$\left(\frac{b}{t_f}\right)_{eq}=\sqrt{\frac{\sigma_{yf}}{E}\left(\frac{b}{t_f}\right)^2+\frac{1}{C}\frac{\sigma_{yw}}{E}\left(\frac{d}{t_w}\right)^2} \quad C\text{=22 (columns), 41 (beams)} \tag{1}$$

In addition, the new width-thickness ratio, W_f, is proposed by Ikarashi et al. [12] as an evaluation index of I-shaped beams, as shown in Eqs. (2), (3), and (4). This research attempts to apply the evaluation of beams subjected to the horizontal force and alternating axial forces.

$$W_f=\sqrt{\frac{1}{k^2}\left(\frac{d/t_w}{\sqrt{E/\sigma_{yw}}}\right)^2+\left(3.43-\frac{25.0}{k^2}\left(\frac{b/t_f}{\sqrt{E/\sigma_{yf}}}\right)^2\right)} \tag{2}$$

where

$$k = \begin{cases} 4.4 & \alpha < 1/6 \\ 5.18 - 4.6\alpha & 1/6 < \alpha < 1/2 \\ 2.9 & \alpha > 1/2 \end{cases} \quad (3)$$

$$\alpha = \left(\frac{1}{6} + \frac{A_f}{A_w} \right) \frac{\beta}{\lambda_w} \quad (4)$$

where A_f is the flange cross sectional area, A_w is the web cross sectional area, β is the gradient of the flexural moment, and λ_w is the web aspect ratio. The slenderness ratio of the numerical model is classified as L-I [17].

Fig. 8 shows the classification of the width-thickness ratio guided by the Architectural Institute of Japan. The gray lines are the classification for beams (P-I-1, P-I-2, and P-II), and the black lines are the classification for columns (P-I-1, P-I-2, and P-II). Ref. 17) assures us that the beams classified as P-I-1 possess the plastic deformation capacity ($\mu'_{max} = \theta_{max}/\theta_p$ -1), $\mu'_{max} \geq 4$, P-I-2 possesses, $\mu'_{max} \geq 2$, P-II possesses, $\mu'_{max} \geq 0$, where θ_{max} is the rotation at ultimate flexural strength and θ_p is the yield rotation ($=M_p/(3EI/L)$). All specimens in this research belong to P-I-1 or P-II in the beam classification scheme, and P-I-1 to P-III in the column classification scheme.

The magnitude of the axial force ratio varies from 0 to 0.3 with an interval of 0.05. The number of loading cycles in each loading amplitude is one or two cycles. The two cycles of loading are conducted only at n=0, 0.15, and 0.3. The yield strength is fixed as 300 N/mm^2 regardless of the plate thickness to target the influence of beam sections and the magnitude of the axial force on the structural performance.

2.3 Local Buckling Behavior of I-shaped Beams under Alternating Axial Forces

Fig. 9 shows the hysteresis curves of I-shaped beams under the cyclic loading. Black solid lines depict analytical results, and gray dotted lines illustrate experimental results. Figs. 9(a) and (b) are the hysteresis curves obtained from the beam section with H-300×150×6×9. Fig. 9(a) is under no axial force, and Fig. 9(b) is under alternating axial force, whose magnitude is 30% of the yield axial force. Figs. 9(c) and (d) are the hysteresis curves obtained from the beam section with H-300×125×6×9. Fig. 9(c) is

under no axial force, and Fig. 9(d) is under alternating axial force, whose magnitude is 30% of the yield axial force. The vertical axis and horizontal axis are normalized by the full plastic bending moment M_p, which neglects the influence of axial force and yield rotation θ_p ($=M_p/(3EI/L)$), respectively. Symbols (triangle or inverted triangle) give maximum bending moment in numerical analyses and experiments, respectively.

In Fig. 9(a), the strength deterioration due to the local buckling on the flange and the web occurs at θ/θ_p=2.5 in the cycle of θ/θ_p=4, and another side of the flange originates the local buckling at θ/θ_p=-2.0 in the cycle of θ/θ_p=4. In contrast, as given in Fig. 9(b), although the local buckling originates at θ/θ_p=-1.4 under the compressive axial force (negative side loading) in the cycle of θ/θ_p=2, the residual deformation is stretched by tensile axial force (positive side loading) and bending moment increases up to the final loading cycle (θ/θ_p=6). Figs. 9(c) and (d) show the same characteristics as Figs. 9(a) and (b). As a result, the ultimate strength and hysteretic energy dissipation under the alternating axial force become larger than the ultimate strength and hysteretic energy dissipation under the constant compressive axial force.

From Fig. 9, the strength deterioration is more severe in the wider beam width (B=150mm) than in 125 mm of beam width regardless of the existence of the axial force. In addition, the amount of energy dissipation and flexural stiffness in the positive side loading in 150 mm of beam width decrease than in 125mm of beam width.

The numerical model grasps the ultimate strength and deflection angle when the beam reaches the ultimate strength, the gradient of strength deterioration, and the pinching effect under the tensile axial force, proving the validity of the analysis model.

Fig. 10 displays the residual deformation (θ/θ_p=6) under no axial force and n=0.3 obtained from the cyclic loading tests and numerical analyses in H-300×150×6×9. The local buckling can be confirmed to occur on the compressive side of the flange in cyclic loading tests and numerical analyses, both under no axial force and n=0.3. The web buckling also originates with the local buckling of the flange. The

residual deformation appears on both sides of the flange under no axial force. However, the residual deformation on the flange, which is subjected to compressive stress due to bending on the positive side loading, decreases than under no axial force, whereas its magnitude is almost the same on the negative side loading under the alternating axial force. The deformation of the web buckling slightly enlarges due to the compressive axial force, as shown in Fig. 10.

Fig. 11 illustrates the distribution of out-of-plane strain along the beam axis obtained from cyclic loading tests and numerical analyses in the cycle of θ/θ_p=4. The out-of-plane strain is calculated as a remainder between left and right sides of the in-plane strain on a flange plate. The in-plane strain is computed by removing the plate bending through averaging the axial strain on both sides of the flange plate. Figs. 11(a) and (b) are the cases of no axial force and n=0.3, respectively. A small out-of-plane strain originates in H-300×150×6×9 (No. 2), whereas 0.5% and 4.0% of out-of-plane strain under no axial force and n=0.3 originates in H-300×125×6×9 (No. 8) at a maximum, indicating that beams with slender sections tend to collapse with combined (local and lateral-torsional) buckling near the fixed end.

Fig. 12 shows the contour figures of out-of-plane deformation under n=0.3 in the cycle of θ/θ_p=6. Figs. 12(a) and (b) are obtained from H-300×150×6×9 (No. 2) and H-300×125×6×9 (No. 8), respectively. In Figs. 12 (a-2) and (b-2), the out-of-plane deformation is constrained at 0.25 L from the fixed end. With regard to the position of the out-of-plane deformation, it can be assumed to be 0.3 L to 0.4 L based on the optimum bracing position, which switches the first buckling mode to the secondary mode, derived by Kimura and Yoshino [19]; previous cyclic loading tests on I-shaped beams collapsed with the local buckling in the tests conducted by Ikarashi et al. [20]; and the wavelength of local buckling along the beam axis obtained from the strain distribution on the flange reported by Kimura [11] under no axial force. In addition, under compressive axial force, the preliminary analyses confirm that the wavelength of the local buckling becomes shorter, and the out-of-plane deformation due to the lateral-torsional buckling tends to be larger than that under no axial force. Therefore, the position of constraint for out-of-plane deformation is determined as 0.25 L, which is nearer to the fixed end than the optimum bracing position

by Kimura and Yoshino [19] and cyclic loading tests by Ikarashi et al. [20]. In Fig. 12(a), H-300×150×6×9 (No. 2), which possesses a larger flange width, originates local buckling only, regardless of the existence of out-of-plane constraint, whereas H-300×125×6×9 (No. 8), which possesses a smaller flange width, shows lateral deformation from the fixed end to 0.25 L and originates the combined buckling in Fig. 12(b-1). In contrast, an I-shaped beam with out-of-plane constraint gives the local buckling only in Fig. 12(b-2).

Fig. 13 investigates the influence of out-of-plane constraint on skeleton curves. Figs. 13(a) and (b) display the skeleton curves on the negative side loading (under compressive axial force) arranged by the magnitude of the axial force ratio in H-300×150×6×9 (No. 2) and H-300×125×6×9 (No. 8), respectively. The skeleton curve is drawn by connecting the skeleton parts, where the hysteresis curve exceeds the maximum strength in the previous loading cycle, with reference to Kimura's experiment [11]. In addition, after the strength deterioration occurs, the skeleton parts, which dip below the strength at the unloading point in the previous loading cycle, are coupled. The vertical axis and the horizontal axis are normalized by the full plastic bending moment M_{pc}, which considers the influence of the axial force and corresponding yield rotation θ_{pc} ($=M_{pc}/(3EI/L)$), respectively. Fig. 13 also depicts the skeleton curves obtained from the numerical model under one time loading in each loading cycle. The skeleton curves of H-300×150×6×9 (No. 2), which has a wider flange width, are almost the same regardless of the existence of out-of-plane constraint. On the other hand, the ultimate strength and plastic deformation capacity decrease when the out-of-plane constraint does not exist in H-300×125×6×9 (No. 8), which possesses a smaller flange width. The difference between both results becomes larger when the axial force is applied on the beam, proving that the structural performance of the beam collapsed with combined buckling decreases than the collapse with dominant local buckling.

In this paper, the out-of-plane constraint is installed at 0.25 L from the fixed end to investigate the structural performance governed by the local buckling. Additionally, the experimental result obtained from H-300×150×6×9, which collapses with the local buckling, is considered below.

3. Evaluation for Structural Performance of I-shaped Beams under Alternating Axial Forces Collapsed with Local Buckling

3.1 Ultimate Strength, Plastic Deformation Capacity, and Cumulative Plastic Deformation Capacity

In this section, the structural performance is evaluated based on the numerical results of I-shaped beams with out-of-plane constraint at 0.25 L from the fixed end.

Fig. 14 shows the relationship between the structural performance and magnitude of the axial force. Figs. 14(a), (b), and (c) illustrate the ultimate strength ratio τ_{cmax} (=M_{max}/M_{pc}), plastic deformation capacity μ'_{cmax} (= (θ_{max}/θ_{pc}) - 1), and cumulative plastic deformation capacity η_{cmax} (=1+(τ_{cmax}+1)(μ'_{cmax}-1)/2), which is the normalized area of the skeleton curve up to the ultimate strength [13]. In Fig. 14, the structural performance can be confirmed to deteriorate with the increase in the magnitude of the axial force, although their values are inconsistent, depending on the beam sections even under the same magnitude of axial force. "Recommended Provisions for Seismic Damping Systems Applied to Steel Structures" [3] published by the Architectural Institute of Japan is defined to apply the width-thickness ranks of the columns for the beams subjected to equal to or greater than 15% of the compressive axial force to the yield axial force [3]. Ref. 17) assures us that the beams classified as P-I-1 possess $\mu'_{max} \geq 4$, P-I-2 possesses $\mu'_{max} \geq 2$, and P-II possesses $\mu'_{max} \geq 0$. Fig. 14(b) displays the plastic deformation capacity of H-300×150×8×10 (No.5) and H-300×125×8×10 (No.10), which are classified as P-I-2 in columns, exceeding 4, which satisfies the criteria of P-I-1, under n=0.3. However, the plastic deformation capacity under n=0.15 surpasses 4 in all numerical models except H-300×150×5×9 (No.1), although they are categorized as P-III in columns. This trend indicates that "Recommended Provisions for Seismic Damping Systems Applied to Steel Structures" guides the conservative criteria for beams in braced structures [3].

Fig. 15 depicts the relationship between the equivalent width-thickness ratios and the structural performance of beams. Figs. 15(a), (b), and (c) show the ultimate strength ratio, plastic deformation

capacity, and cumulative plastic deformation capacity, respectively. The horizontal axis is the equivalent width-thickness ratio calculated by Eq. (1). The structural capacities of beams degrade with the increase in the equivalent width-thickness ratio. The plastic deformation capacity exceeds 4 when the equivalent width-thickness ratio is smaller than 0.42 under n=0.15 and 0.32 under n=0.3. However, the evaluation formulae cannot be proposed directly since the ultimate strength ratio, plastic deformation capacity, and cumulative plastic deformation capacity differ depending on the magnitude of axial force among the same equivalent width-thickness ratio. In addition, the plots scatter approximately 0.34 to 0.4 in the equivalent width-thickness ratio under n=0.3 in Figs. 15(a), (b), and (c).

Therefore, this section investigates the structural performance of I-shaped beam with different web thickness ratios and flange thickness ratios within the same equivalent width-thickness ratio. Fig. 16 gives the skeleton curves of beams which possess different web thickness and flange thickness among the same equivalent width-thickness ratio. The skeleton curves on the negative side (under compressive axial force) are drawn as in Fig. 13. The vertical axis and the horizontal axis are normalized by the full plastic bending moment, M_{pc}, and corresponding yield rotation θ_{pc} ($=M_{pc}/(3EI/L)$), respectively. Fig 16(a) compares between H-300×150×6×9 (No. 2) and H-300×125×6×7.5 (No. 7), whose equivalent width-thickness ratio is 0.42, and Fig. 16(b) is for H-300×150×6×12 (No. 4) and H-300×150×8×10 (No. 5), whose equivalent width-thickness ratio is 0.36. In Fig. 15(a), the skeleton curves match with each other regardless of the magnitude of the axial force. In contrast, the ultimate strength ratio and plastic deformation capacity of H-300×150×6×12 (No. 4), which possesses a larger web-thickness ratio, become less than the ultimate strength ratio and plastic deformation capacity of H-300×150×8×10 (No. 5). The gaps between the beam sections are 7%, 79%, and 87% in the ultimate strength ratio, plastic deformation capacity, and cumulative plastic deformation capacity, respectively. Although the equivalent width-thickness ratio calculated by Eq. (1) considers the contribution of the flange width-thickness ratio and web width-thickness ratio uniformly, irrespective of the magnitude of the axial force, the ultimate strength ratio, plastic deformation capacity, and cumulative plastic deformation

capacity deteriorate when the I-shaped beams have a large flange-thickness ratio as the web local buckling can originate in smaller deformations, indicating the necessity to reset the influence of the web width-thickness ratio in the equivalent width-thickness ratio under a large axial force.

3.2 Validity of Previous Evaluation Formulae and Application of Equivalent Width-thickness Ratio Considering Compressive Axial Force

Fig. 17 illustrates the comparison between the predicted values by Ikarashi [14] and analytical results, experimental results in this paper, and previous experimental results by Kimura [11]. The ultimate strength ratio and plastic deformation capacity in Figs. 17(a) and (b) are calculated with a new width-thickness ratio, W_f, and cumulative plastic deformation capacity in Fig. 17(c) is obtained as $\eta_{cmax}=1+(\tau_{cmax}+1)(\mu'_{cmax}-1)/2$ using the ultimate strength ratio and plastic deformation capacity with reference to Kimura's research [11]. In Figs. 17(a) and (b), almost all ultimate strength ratios and plastic deformation capacities exceed the predicted values because Ikarashi et al. [14] set the evaluation formulae as the lower bound of experimental and analytical results. The assessed numbers agree with numerical and experimental values in the smaller region of the ultimate strength ratio and plastic deformation capacity. However, the conservativism is enlarged in the larger region, assuming that the previous formulae cannot be applied to the alternating axial forces, as Ikarashi et al. [14] targets the constant compressive axial force.

Fig. 18 shows the comparison of skeleton curves of H-300×150×6×9 and H-300×125×6×9 under a constant compressive axial force and alternating axial forces. The ultimate strength ratio, plastic deformation capacity, and cumulative plastic deformation capacity under the alternating axial forces may be 1.1 times (H-300×150×6×9, n=0.15), 2.1 times (H-300×150×6×9, n=0.15), or 2.2 times (H-300×150×6×9, n=0.15) higher than those parameters under the constant compressive axial force, respectively, because the residual deformation of local buckling is stretched by the tensile axial force. Thus, the evaluation formulae [14] of Ikarashi underestimate the numerical and experimental results under alternating axial forces.

Therefore, this chapter establishes the evaluation formulae for the ultimate strength ratio, plastic deformation capacity, and cumulative plastic deformation capacity considering the influence of the axial force based on Kimura's report [11]. Fig. 15 and Fig. 16 display the inconsistency of the relationship between structural performance of beams and equivalent width-thickness ratios under the large magnitude of the axial force, which evinces the necessity to reset the influence of the web-thickness ratio. The modified equivalent width-thickness ratio is therefore proposed to estimate the analytical and experimental results in Eqs. (5) and (6).

$$\left(\frac{b}{t_f}\right)_{eq}' = \sqrt{\frac{\sigma_{yf}}{E}\left(\frac{b}{t_f}\right)^2 + \frac{1}{C}\frac{1}{1-n'}\frac{\sigma_{yw}}{E}\left(\frac{d}{t_w}\right)^2} \tag{5}$$

$$n' = \frac{N_{max}}{N_{y,web}} < 1 \tag{6}$$

where N_{max} is the maximum axial force and $N_{y,web}$ is the web yield axial force. Here, the coefficient C is defined as 41 since this paper focuses on beams.

Fig. 19 gives the ultimate strength ratio, plastic deformation capacity, and cumulative plastic deformation capacity obtained from numerical analyses and experiments arranged by the modified equivalent width-thickness ratio. Figs. 19(a), (b), and (c) are the ultimate strength ratio, plastic deformation capacity, cumulative plastic deformation capacity, respectively. Symbols depict the experimental and numerical results in this paper, and the experimental values collapsed with the local buckling in Kimura's experiment [11] are also included in Figs. 19(a), (b), and (c).

The modified equivalent width-thickness ratio can arrange the structural performance of the I-shaped beams under the alternating axial forces with less scatter regardless of the beam sections and magnitude of the axial force ratio.

Based on the findings above, the evaluation formulae for the ultimate strength ratio, plastic deformation capacity, and cumulative plastic deformation capacity are proposed as Eqs. (7), (8), and (9) by replacing the width-thickness ratio of previous formulae in Kimura's research [11] by the modified equivalent

width-thickness ratio. In addition, the scope of application of Eqs. (7), (8), and (9) is fixed as $(b/t_f)_{eq}' \leq 0.68$ as structural performance does not become negative values.

$$\tau_{cmax} = \left[1.1 + \left(\frac{0.07}{(b/t_f)_{eq}' - 0.2} - 0.01L/H\right)\right]\left(1.1 - \frac{0.1N}{\sum \mu_{xi}}\right) \tag{7}$$

$$\mu'_{cmax} = \left[-6.2 + \left(\frac{2.5}{(b/t_f)_{eq}' - 0.2} + \frac{4.5}{L/H}\right)\right]\left(0.55 - \frac{0.08\sum \mu_{xi}}{N}\right) \tag{8}$$

$$\eta_{cmax} = \frac{(\tau_{cmax} + 1)(\mu'_{cmax} + 1 - \tau_{cmax})}{2} \tag{9}$$

The proposed formulae are illustrated in Fig. 19. The error rates are indicated as ±10% in Fig. 19(a) and ±30% in Figs. 19(b) and (c) as the lower and upper bounds. In Fig. 19, the I-shaped beams under the alternating axial forces satisfy the required plastic deformation capacity of P-I-1 ($\mu'_{max} \geq 4$) and P-I-2 ($\mu'_{max} \geq 2$) in "Recommendation for Limit State Design of Steel Structures" [17] published by the Architectural Institute of Japan when the modified equivalent width-thickness ratio is smaller than 0.43 and 0.50, respectively.

Fig. 20 illustrates the structural performance obtained from numerical analyses, experiments, and Kimura's experiment [11] arranged by the modified W_f, W_f', which considers the influence of the axial force on the web width-thickness ratio. The equation of W_f' is shown in Eq. (10).

$$W_f' = \sqrt{\frac{1}{1-n'}\frac{1}{k^2}\left(\frac{d/t_w}{\sqrt{E/\sigma_y}}\right)^2 + \left(3.43 - \frac{25.0}{k^2}\left(\frac{b/t_f}{\sqrt{E/\sigma_y}}\right)^2\right)} \tag{10}$$

The coefficients k and α are obtained by Eqs. (3) and (4), respectively. Figs. 19(a), (b), and (c) show the ultimate strength ratio, plastic deformation capacity, and cumulative plastic deformation capacity, respectively. All structural performance have a negative relationship with W_f', and the scatter is found to be smaller than in Figs. 15(a), (b), and (c). The applicable scope range is determined as $W_f' \leq 1.5$, which corresponds to 0.68 in the modified equivalent width-thickness ratio.

3.3 Bauschinger Effect Coefficient and Hysteretic Energy Dissipation

Fig. 21 illustrates the relationship between the Bauschinger effect coefficient, α_b, of I-shaped beams under the alternating axial forces and number of loading cycles and cumulative loading amplitude. The Bauschinger effect coefficient is defined as the proportion of hysteretic energy dissipation in the cumulative hysteresis curve to the cumulative plastic deformation capacity in the skeleton curve. Ref. 21) guides us to set the Bauschinger effect coefficient as a constant, 2.0 for beams and 1.67 for columns. However, Kimura revealed that the Bauschinger effect coefficient relates to the number of loading cycles and cumulative loading amplitude, and the coefficient can be evaluated by the equation below [11]. In addition, the vertical axis in Fig. 21 is the second term of Eq. (11).

$$\alpha_B = 1 + 0.5(N-1)\log\sqrt{\sum_{i=1}\mu_{xi}} \tag{11}$$

where N is the number of loading cycles and $\Sigma\mu_{xi}$ is the cumulative normalized loading amplitude. Although N becomes 0.5 (half cycle) under the monotonic loading, this research determines N as the same as Kimura's research [11]. The only first loading is counted when the loading remains in the elastic region during the cyclic loading. This research also applies Eq. (11) to the beams under the alternating axial forces and investigates its validity. The experimental results collapsed with the local buckling in Kimura's experiment [11] are also given in Fig. 21. The Eq. (11) is illustrated by a dashed line in Fig. 21. The Bauschinger effect coefficient increases with enlargement of the number of loading cycles and cumulative normalized loading amplitude and is roughly estimated by Eq. (11).

Therefore, the hysteretic energy dissipation of I-shaped beams under the alternating axial forces can be calculated as a product of cumulative energy dissipation, η_{cmax}, in Eq. (9) and the Bauschinger effect coefficient, α_b, in Eq. (11). Fig. 22 displays the comparison of the hysteretic energy dissipation obtained from evaluation formulae and the numerical analyses and experiments. The predicted values agree with the analytical and experimental results. The hysteretic energy dissipation under the compressive axial force, therefore, can be estimated by the proposed formulae in this research.

Next, the hysteretic energy dissipation under the tensile axial force is investigated. Fig. 23 gives the comparison of the hysteretic energy dissipation of the I-shaped beams under compressive axial force and

tensile axial force. The vertical axis and the horizontal axis are the positive side loading (tensile axial force) and negative side loading (compressive axial force), respectively. The hysteretic energy dissipation in the second loading under two cycles of loading in each loading amplitude is targeted in this comparison. The hysteretic energy dissipation is almost the same in the small and mid-magnitude loading amplitudes (θ/θ_p=1, 2, 4, 6). However, the hysteretic energy dissipation on the positive side loading becomes greater than the hysteretic energy dissipation on the negative side loading in the large magnitude of loading amplitude (θ/θ_p=8, 10) under no axial force because the local buckling originates on the negative side loading, while it does not happen on the positive side loading.

However, the hysteretic energy dissipation under the alternating axial force is almost the same in the positive (tensile axial force) and negative (compressive axial force) side loading, explained by the hysteresis curve in Fig. 24. Figs. 24(a) and (b) illustrate the hysteresis curves in the positive and negative side loading under n=0.15 and n=0.3 in θ/θ_p=6, respectively. The I-shaped beam under the alternating axial forces originates the strength deterioration due to local buckling under the compressive axial force, whereas the pinching, which gives a smaller flexural gradient, happens under the tensile axial force. Thus, the hysteretic energy dissipation on both sides of the loading do not differ from each other. The obtained energy dissipation under compressive axial force, therefore, can be applied to the obtained energy dissipation under the tensile axial force.

4. Summary and Conclusion

In this chapter, the ultimate strength ratio, plastic deformation capacity, cumulative plastic deformation capacity, and hysteretic energy dissipation under the compressive axial force are evaluated through cyclic loading tests and numerical analyses on the I-shaped beams connected with buckling restrained braces. The obtained findings are summarized as follows.

1) The ultimate strength ratio, plastic deformation capacity, and cumulative plastic deformation capacity of I-shaped beam collapsed with the local buckling under the alternating axial forces

degrade with the increase in the magnitude of the axial force ratio. The required plastic deformation capacity for P-I-1 can be secured when the equivalent width-thickness ratio is less than 0.42 under n=0.15 and 0.32 under n=0.3.

2) The ultimate strength ratio, plastic deformation capacity, and cumulative plastic deformation capacity of I-shaped beams under the alternating axial forces are assessed regardless of the beam sections and magnitude of the axial force ratio by the modified equivalent width-thickness ratio, which considers the proportion of the axial force to web yield axial strength as a coefficient. The structural performance above is predicted by the proposed formulae employing the modified equivalent width-thickness ratio as shown in Eqs. (7), (8), and (9). In addition, the modified W_f, which is capable of estimating the structural capacities, can be calculated using the same coefficient as the modified equivalent width-thickness ratio.
3) The Bauschinger effect coefficient of I-shaped beams under the alternating axial forces increases with enlargement of the number of loading cycles and normalized cumulative loading amplitude the same as under no axial force. In addition, the coefficient can be assessed by Eq. (11). The hysteretic energy dissipation of I-shaped beams under compressive axial force is, therefore, calculated as a product of the cumulative plastic deformation capacity (Eq. (9)) and the Bauschinger effect coefficient (Eq. (11)).
4) The total hysteretic energy dissipation is obtained by doubling the hysteretic energy dissipation under compressive axial force since the hysteretic energy dissipation under the tensile axial force is almost the same as under the compressive axial force.

Acknowledgements

This research was funded by a grant from the Award of Applied Ceramics Laboratories of Tokyo Institute of Technology “Evaluation of Seismic Capacity of Steel Structures with Different Frame Systems” (Award Winner: Yoshihiro Kimura) and a grant from The Japan Iron and Steel Federation

(Principal Investigator: Atsushi Suzuki). The series of experiments was conducted by Dr. Teruaki Yamanishi at the Hiroshima Institute of Technology. The authors would like to express special thanks to the funding source and the contributions.

Disclosure

The authors have no conflict of interest to declare.

References

1) Satoshi Takahashi, Shoichi Kishiki, and Akira Wada. “Experimental studies and investigations regarding usage of buckling restrained brace in present structures”, *Proceeding of the architectural research meetings in Kanto chapter*, pp. 233-236, 2008.2 (in Japanese)

2) Toru Takeuchi, Mari Ida, Satoshi Yamada, and Kazuaki Suzuki. “Estimation of cumulative deformation capacity of buckling restrained braces, *Journal of Structural Engineering*, pp. 822-831, 2008.5

3) Architectural Institute of Japan. “*Recommended Provisions for Seismic Damping Systems applied to Steel Structures*”. 2014.11 (in Japanese)

4) Ben Kato, Hiroshi Akiyama, and Yoichi Obi. “Deformation Characteristics of H-shaped Steel Members Influenced by Local Buckling”, *Journal of Structural and Construction Engineering (Transactions of AIJ)*, Architectural Institute of Japan, No. 257, pp.49-58, 1977.7 (in Japanese)

5) Toshiro Suzuki and Kenichiro Tamamatsu. “Experimental Study on Energy Absorption Capacity of Columns of Low Steel Structures Part 1 Energy Absorption Capacity of H-shaped Steel Columns Subjected to Monotonic Loading and Cyclic Loading with Constant Deflection Amplitudes”, *Journal of Structural and Construction Engineering (Transactions of AIJ)*, Architectural Institute of Japan, No. 279, pp.65-78, 1979.5 (in Japanese)

6) Minoru Yamada, Bunzo Tsuji, and Yasunori Ijiri. “Collapse Characteristics and Shear Deformation

of H-shaped Columns Subjected to Double Curveture Bending", *Proceeding of the architectural research meetings in Kinki chapter*, pp. 221-224, 1982.6 (in Japanese)

7) Bunzo Tsuji, Toru Hashimura, Kazushi Shirakawa. "Elasto-Plastic Deformation and Fracture Behaviors of Wide Flange Beam-Columns Subjected to Double Curvature Bending under Constant Axial Load", *Proceeding of the architectural research meetings in Kinki chapter*, pp. 201-204, 1983.6 (in Japanese)

8) Minoru Yamada, Shigeru Kawamura, Isao Taniaki, Kazuhiro Yagi. "Collapse Characteristics and Shear Deformation of H-shaped Columns Subjected to Double Curvature Cyclic Bending", *Proceeding of the architectural research meetings in Kinki chapter*, pp. 209-212, 1983.6 (in Japanese)

9) Bunzo Tsuji, Takahito Nishino, Makoto Ogawara. "Elastic Plastic Deformation and Collapse Behavior of Wide Flange Column", *Proceeding of the architectural research meetings in Kinki chapter*, pp. 361-364, 1984.6 (in Japanese)

10) Bunzo Tsuji, Takahito Nishino Toru Hashimura. "Elastic Plastic Shear Deformation and Collapse Behavior of Wide Flange Short Column", *Proceeding of the architectural research meetings in Kinki chapter*, pp. 365-368, 1984.6 (in Japanese)

11) Yoshihiro Kimura. "Effect of Loading Hysteretic Program on Plastic Deformation Capacity and Cumulative Plastic Deformation Capacity for H-shaped Beam with Local Buckling", *Journal of Structural and Construction Engineering (Transactions of AIJ)*, Architectural Institute of Japan, Vol. 76, No. 664, pp.1143-1151, 2011.6 (in Japanese)

12) Kikuo Ikarashi, Ryota Suekuni, Takuma Shinohara, and Tao Wang. "Evaluation of Plastic Deformation Capacity of H-shaped Steel Beams with Newly Proposed Limitation Value of Plate Slenderness", *Journal of Structural and Construction Engineering (Transactions of AIJ)*, Architectural Institute of Japan, Vol. 76, No. 668, pp.1865-1872, 2011.10 (in Japanese)

13) Yoshihiro Kimura, Teruaki Yamanishi, and Kazuhiko Kasai. "Cyclic Hysteresis Behavior and Plastic

Deformation Capacity for H-shaped Beams on Local Buckling under Compressive and Tensile Forces", *Journal of Structural and Construction Engineering (Transactions of AIJ)*, Architectural Institute of Japan, Vol. 78, No. 689, pp.1307-1316, 2013.7 (in Japanese)

14) Kikuo Ikarashi and Ryota Hasegawa. "Evaluation Method of Ultimate Strength and Plastic Deformation Capacity of H-shaped Steel Columns", *Journal of Structural Engineering*, Architectural Institute of Japan, Vol. 61B, pp.209-216, 2015.3

15) Kazuhiko Kasai, Yoriyuki Matsuda, Shojiro Motoyui, and Shoichi Kishiki. "Fundamental Study Using New Test Loading Scheme for Steel Frame Subassembly with Damper Connection Details", *Journal of Structural and Construction Engineering (Transactions of AIJ)*, Architectural Institute of Japan, Vol. 80, No. 708, pp.309-319, 2015.2 (in Japanese)

16) Dassault Systèmes. "*ABAQUS/Standard User's Manual version 6.14-5*", 2014.4

17) Architectural Institute of Japan. "*Recommendation for Limit State Design of Steel Structures*", 2010.2 (in Japanese)

18) Akio Kadono, Michio Sasaki, Kentaro Okamoto, Hiroshi Akiyama, Chiaki Matsui, and Kazuo Inoue. "Experimental Study on the Effect of Yield Ratio on the Bending Strength Increasing Ratio and the Ductility of Steel Structures' Method", *Journal of Structural Engineering*, Architectural Institute of Japan, Vol. 40B, pp.673-682, 1994.3

19) Yoshihiro Kimura and Yuki Yoshino. "Effect of Lateral and Rotational Restraint for Bracings on Lateral Buckling Load for H-shaped Beams under Moment Gradient", *Journal of Structural and Construction Engineering (Transactions of AIJ)*, Architectural Institute of Japan, Vol. 79, No. 700, pp.761-770, 2014.6 (in Japanese)

20) Kikuo Ikarashi, Satoshi Miyazaki, Yasuo Ichinohe, Koji Fukuda, Junichiro Ono, and Seiya Kimura. "Plastic Deformation Capacity of H-shaped Beams Reinforced by End Stiffeners", *Journal of Structural and Construction Engineering (Transactions of AIJ)* Architectural Institute of Japan, Vol. 79, No. 705, pp.1667-1675, 2014.11 (in Japanese)

21) Architectural Institute of Japan. "*Ultimate Strength and Deformation Capacity of Buildings in Seismic Design (1990)*", 1990.10 (in Japanese)

22) Morihisa Fujimoto, Atsuhide Hashimoto, Tadao Nakagomi, and Tomohisa Yamada. "*Study on Fracture of Welded Connections in Steel Structures under Cyclic Loads Based on Nonlinear Fracture Mechanics –Part 1 Formulation of Multi-axial Stress-strain Relations of Structural Steel for Cyclic Loads*", *Journal of Structural and Construction Engineering (Transactions of AIJ)*, Architectural Institute of Japan, No. 356, pp.93-102, 1985.10 (in Japanese)

Appendix I. Investigation of the Validity of the Combined Hardening Rule in Numerical Analysis

The validity of the combined hardening rule was investigated through the numerical analysis of the hourglass-shaped specimen. Fig. A-1 shows the numerical model of the hourglass-shaped specimen consisting of 8-noded solid elements. The length of the specimen is 145 mm, and diameters at the center and end of the specimen are 10 mm and 20 mm, respectively. The numerical model in divided into 50 elements along the axis of the specimen, 32 elements along the circumference, and 7 elements along the radius. Fig. A-1 illustrates the deformation at ε=0.05.

Fig. A-2 depicts the comparison of stress-strain curves between the experimental [22)] and numerical results. The experimental and numerical results agree well with each other, and the validity of the numerical model is proven here.

Figure Captions

Fig 1.Loading apparatus

Fig. 2 Concept of the loading test

Fig. 3 Loading protocol for the horizontal force

Fig. 4 Loading protocol for the vertical force

Fig. 5 Position of the displacement and strain gauges

Table 1 List of specimens

Designation	Loading protocol		Magnitude of axial force
	Horizontal	Vertical	
A-1-N	one cycle	no	-
A-1-R0.3	one cycle	alternating	±0.3
A-2-R0.3	two cycles	alternating	±0.3
B-1-N*	one cycle	no	-
B-1-R0.3*	one cycle	alternating	±0.3
B-2-R0.15*	two cycles	alternating	±0.15
B-2-R0.3*	two cycles	alternating	±0.3

Number of cycles for the same displacement amplitude is indicated. The displacement amplitude is increased after completing the cycle.

A - 2 - R0.3
- R0.3: Magnitude of axial force ratio
- R: Protocol of axial force (N: no, R: alternating)
- 2: Number of cycles (1: one, 2: two cyles in one loading amplitude)
- A: Beam section

Beam section	M_p kNm	θ_p rad	M_{pc} kNm	θ_{pc} rad	M_y kNm	N_y kN
A: H-300×150×6×9	178	0.0067	154	0.0058	160	1,546
B: H-300×125×6×9	155	0.0067	136	0.0059	138	1,388

Table 2 Material properties

	Material	E N/mm^2	E_{st} N/mm^2	σ_y N/mm^2	σ_u N/mm^2	ε_u %
PL-6	SS400	204,000	3,100	330	444	14.9
PL-9	SS400	213,000	2,700	352	430	14.7
PL-12	SS400	211,000	2,600	345	430	14.4

E: Young's modulus, E_{st}: strain hardening modulus, σ_y: yield stress, σ_u: ultimate stress, ε_u: strain at σ_u

Table 3 Parameters of the numerical models

No.	Section [mm]				L [mm]	$(b/t_f)_{eq}$		W_f	Classification		Slenderness ratio	Classification	N/N_y	Number of cycles
	H	B	t_w	t_f		Beam	Column		Beam	Column				
1	300	150	5	9	1500	0.46	0.56	0.68	P-I-1	P-III	0.15	L-I	0, 0.05, 0.1, 0.15, 0.2, 0.25, 0.3	one, two (only under N/N_y=0, 0.15, 0.3)
2*	300	150	6	9		0.42	0.50	0.62	P-I-1	P-III	0.17			
3	300	150	6	11		0.39	0.46	0.57	P-I-1	P-III	0.15			
4	300	150	6	12		0.36	0.44	0.54	P-I-1	P-III	0.15			
5	300	150	8	10		0.36	0.40	0.52	P-I-1	P-I-2	0.16			
6	300	125	4.5	9		0.46	0.58	0.68	P-II	P-III	0.18			
7	300	125	6	7.5		0.42	0.50	0.62	P-I-1	P-III	0.19			
8*	300	125	6	9		0.39	0.47	0.56	P-I-1	P-III	0.19			
9	300	125	6	12		0.34	0.42	0.50	P-I-1	P-III	0.18			
10	300	125	8	10		0.32	0.37	0.46	P-I-1	P-I-2	0.19			
11	300	100	6	9		0.35	0.44	0.51	P-I-1	P-III	0.24			

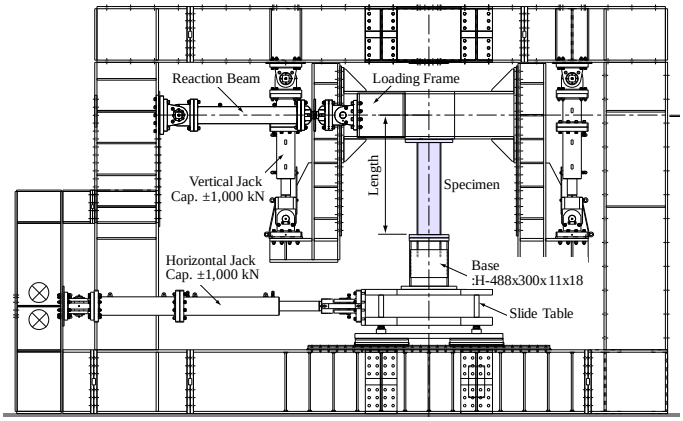
Reaction Beam
Loading Frame
Vertical Jack
Cap. ±1,000 kN
Length
Specimen
Horizontal Jack
Cap. ±1,000 kN
Base
:H-488x300x11x18
Slide Table

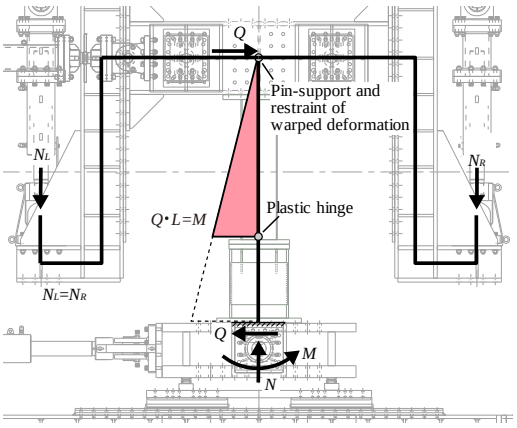
Q
Pin-support and
restraint of
warped deformation
N_L
N_R
Plastic hinge
$Q \cdot L = M$
$N_L = N_R$
Q
M
N

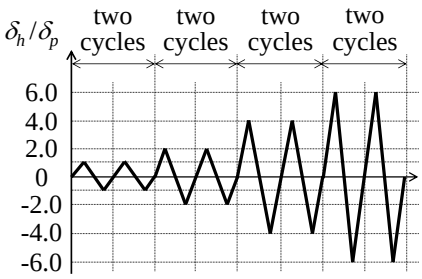
δ_h/δ_p
two cycles
two cycles
two cycles
two cycles
6.0
4.0
2.0
0
-2.0
-4.0
-6.0

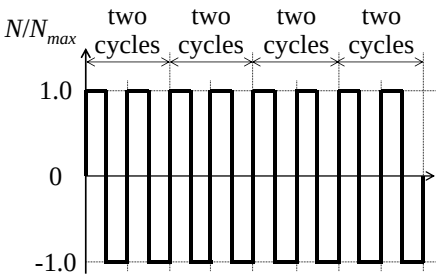
N/N_{max}
two cycles
two cycles
two cycles
two cycles
1.0
0
-1.0

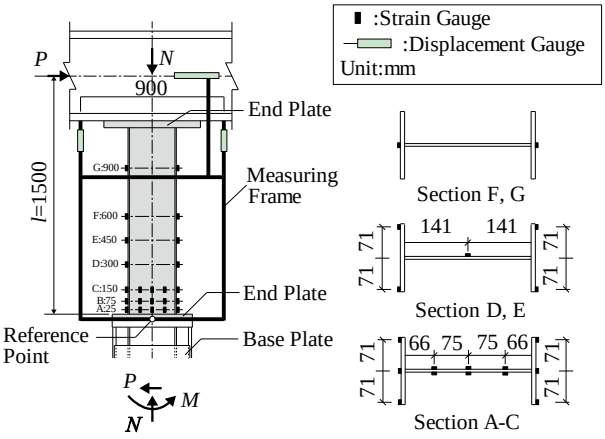
:Strain Gauge
:Displacement Gauge
Unit:mm
P
N
900
End Plate
Measuring Frame
l=1500
G:900
F:600
E:450
D:300
C:150
B:75
A:25
End Plate
Base Plate
Reference Point
P
M
N
Section F, G
141
141
71
71
71
71
Section D, E
66
75
75
66
71
71
71
71
Section A-C

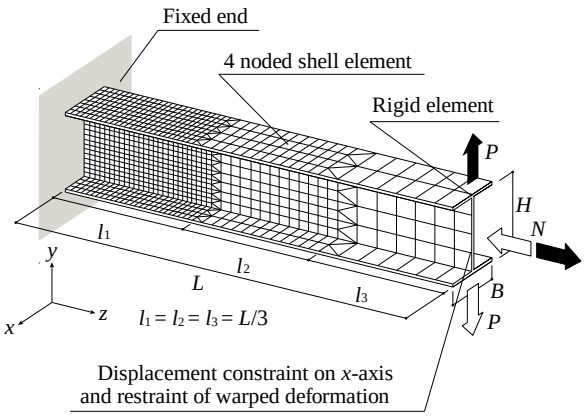
Fixed end
4 noded shell element
Rigid element
P
H
N
B
P
l_1
l_2
l_3
L
y
z
x
$l_1 = l_2 = l_3 = L/3$
Displacement constraint on x-axis
and restraint of warped deformation

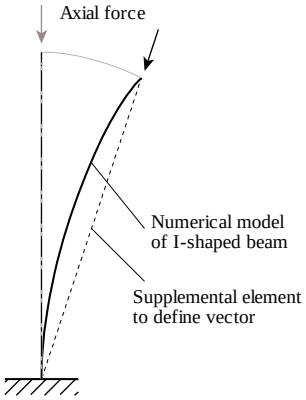
Axial force
Numerical model
of I-shaped beam
Supplemental element
to define vector

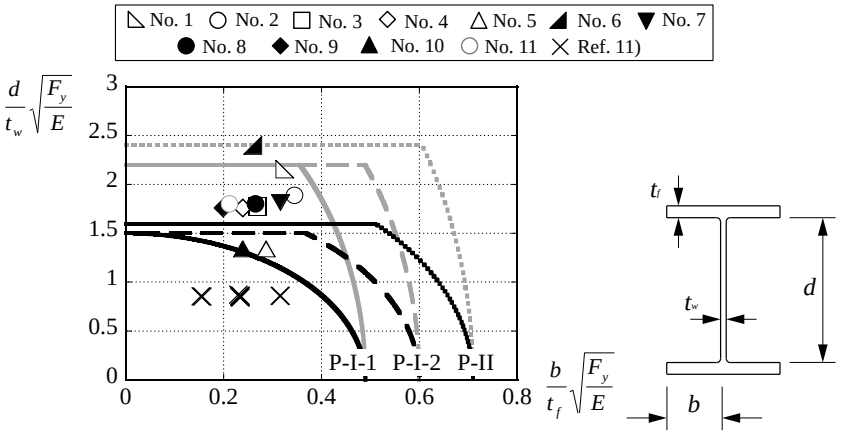
No. 1
No. 2
No. 3
No. 4
No. 5
No. 6
No. 7
No. 8
No. 9
No. 10
No. 11
Ref. 11)
$\frac{d}{t_w}\sqrt{\frac{F_y}{E}}$
3
2.5
2
1.5
1
0.5
0
0
0.2
0.4
0.6
0.8
P-I-1
P-I-2
P-II
$\frac{b}{t_f}\sqrt{\frac{F_y}{E}}$
t_f
t_w
d
b

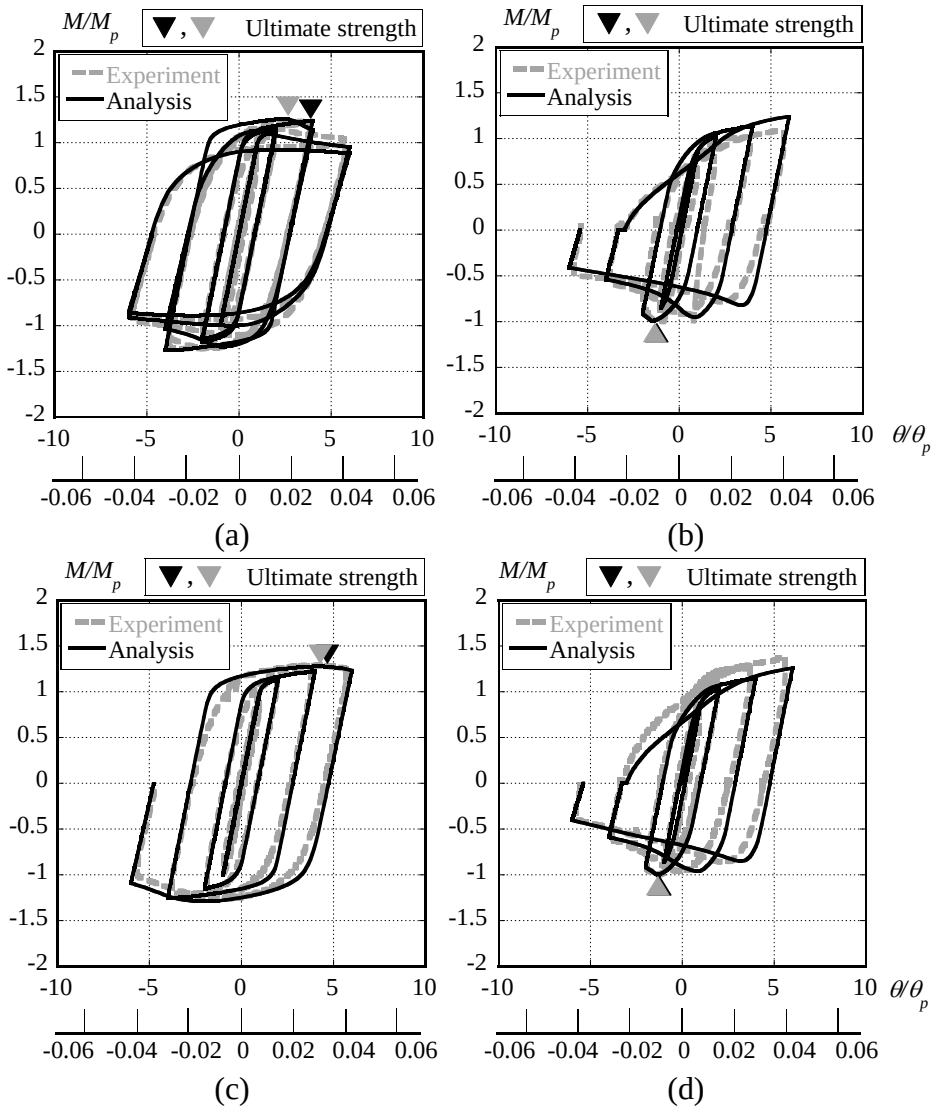
M/M_p
Ultimate strength
Experiment
Analysis
θ/θ_p
(a)
(b)
(c)
(d)

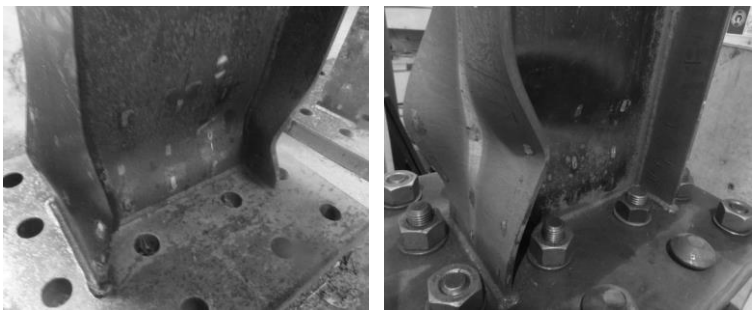

(a) (b)

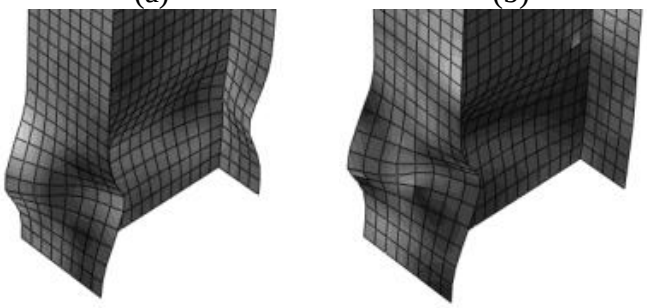

(c) (d)

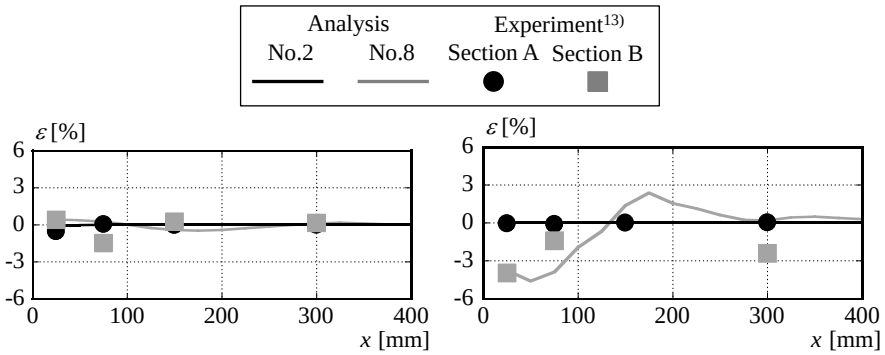
Analysis
No.2
No.8
Experiment[13)]
Section A
Section B
ε [%]
6
3
0
-3
-6
0
100
200
300
400
x [mm]
ε [%]
6
3
0
-3
-6
0
100
200
300
400
x [mm]

(a) (b)

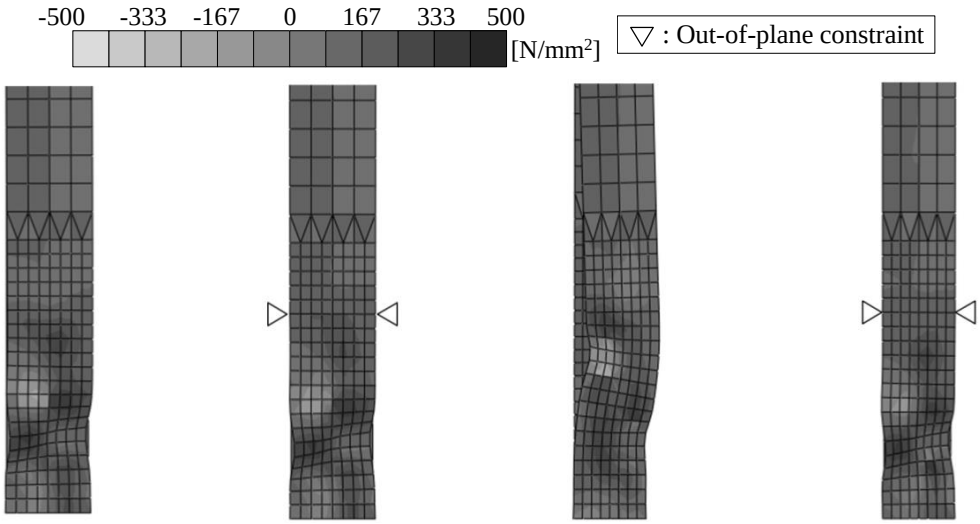
-500 -333 -167 0 167 333 500
[N/mm²]
▽ : Out-of-plane constraint
(a-1)
(a-2)
(b-1)
(b-2)

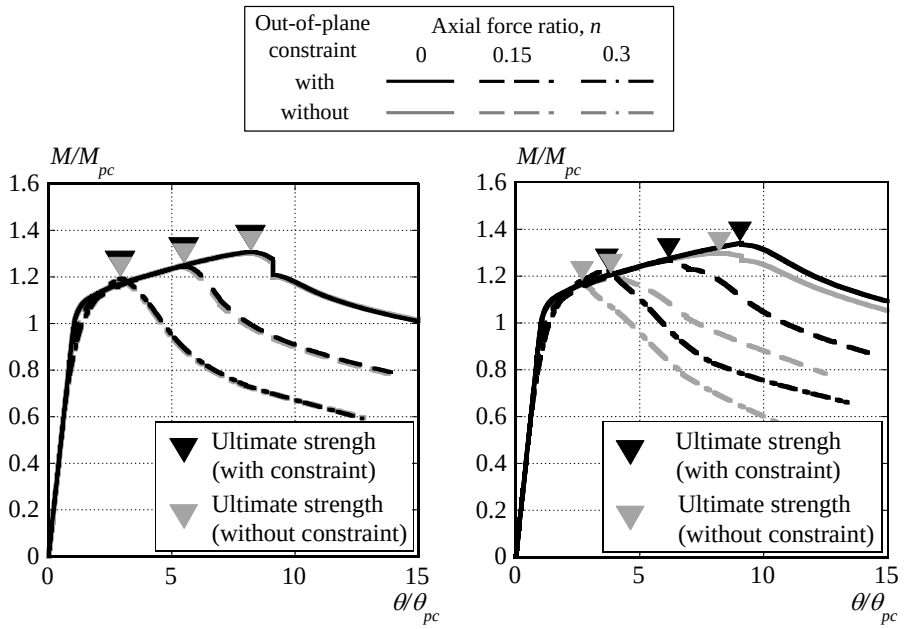
Out-of-plane constraint
Axial force ratio, n
0
0.15
0.3
with
without
M/M_pc
θ/θ_pc
Ultimate strengh (with constraint)
Ultimate strength (without constraint)
(a)
(b)

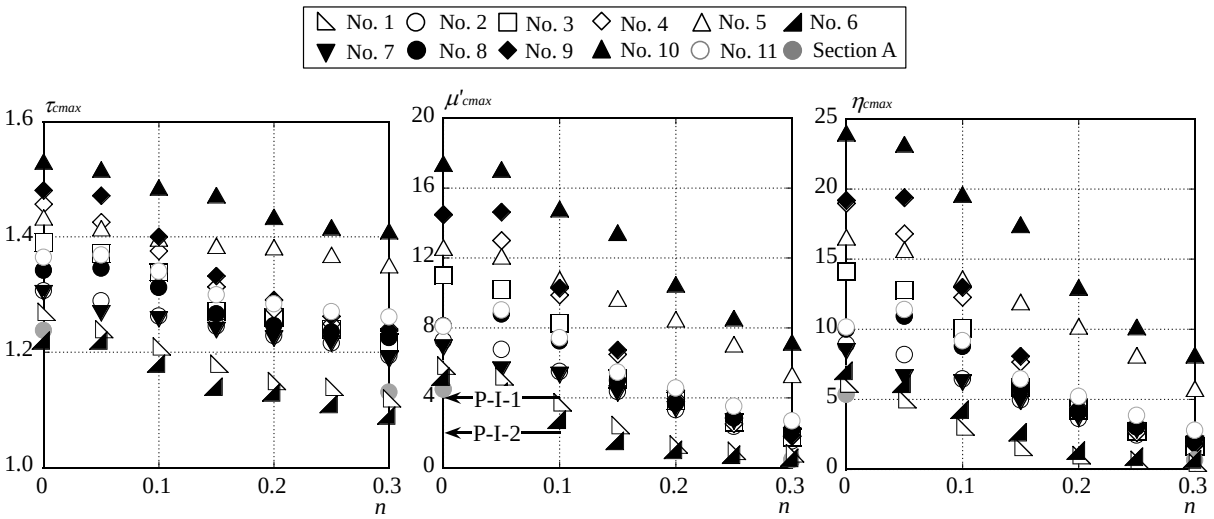
No. 1
No. 2
No. 3
No. 4
No. 5
No. 6
No. 7
No. 8
No. 9
No. 10
No. 11
Section A
τcmax
μ'cmax
ηcmax
P-I-1
P-I-2
n
n
n

(a) (b) (c)

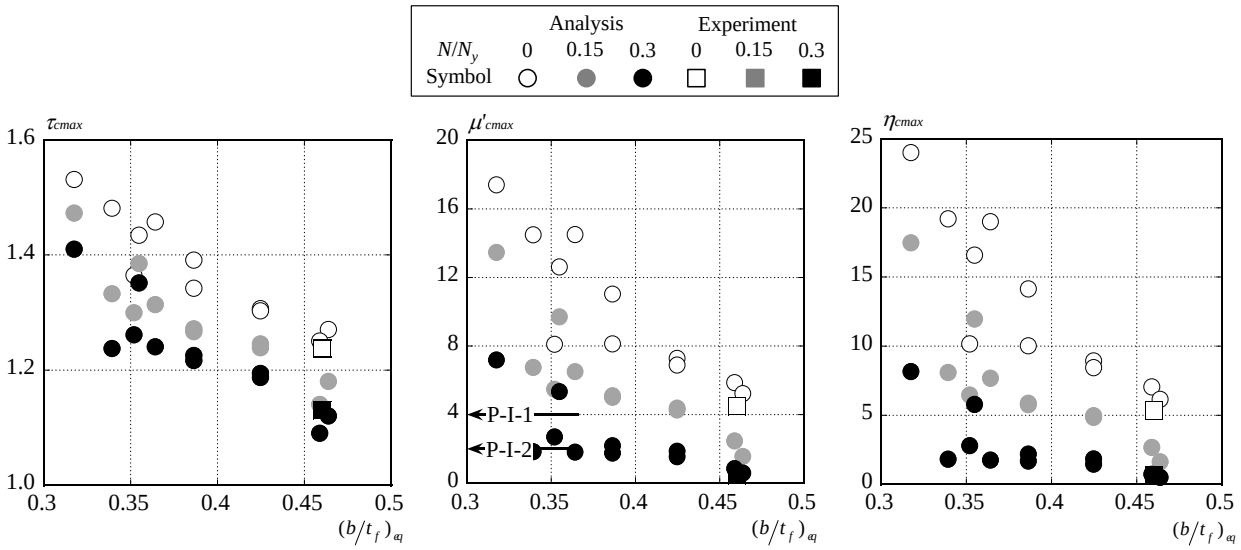
Analysis
Experiment
N/Ny
0
0.15
0.3
0
0.15
0.3
Symbol
τcmax
μ'cmax
ηcmax
P-I-1
P-I-2
(b/tf)eq
(b/tf)eq
(b/tf)eq

(a) (b) (c)

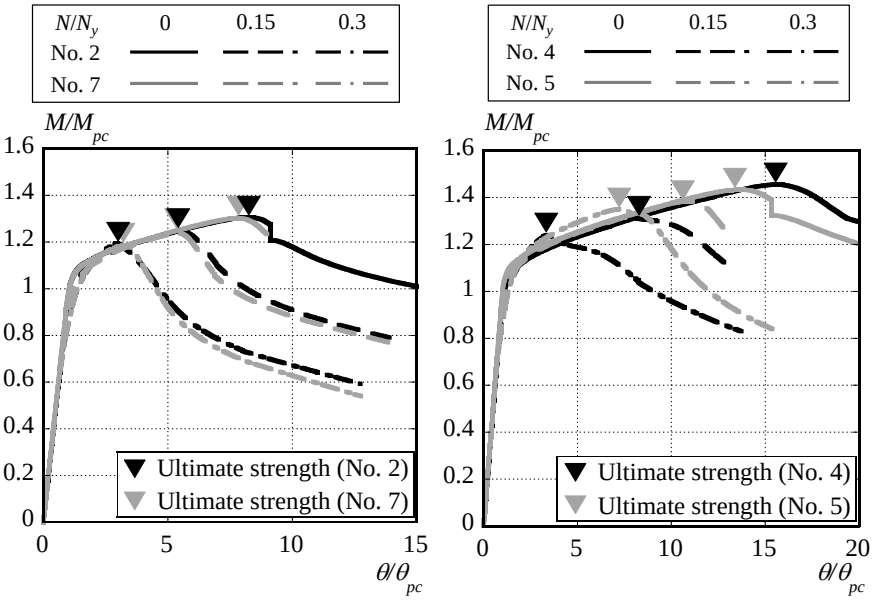
N/N_y 0 0.15 0.3
No. 2
No. 7
M/M_pc
1.6
1.4
1.2
1
0.8
0.6
0.4
0.2
0
0 5 10 15
θ/θ_pc
Ultimate strength (No. 2)
Ultimate strength (No. 7)
N/N_y 0 0.15 0.3
No. 4
No. 5
M/M_pc
0 5 10 15 20
θ/θ_pc
Ultimate strength (No. 4)
Ultimate strength (No. 5)

(a) (b)

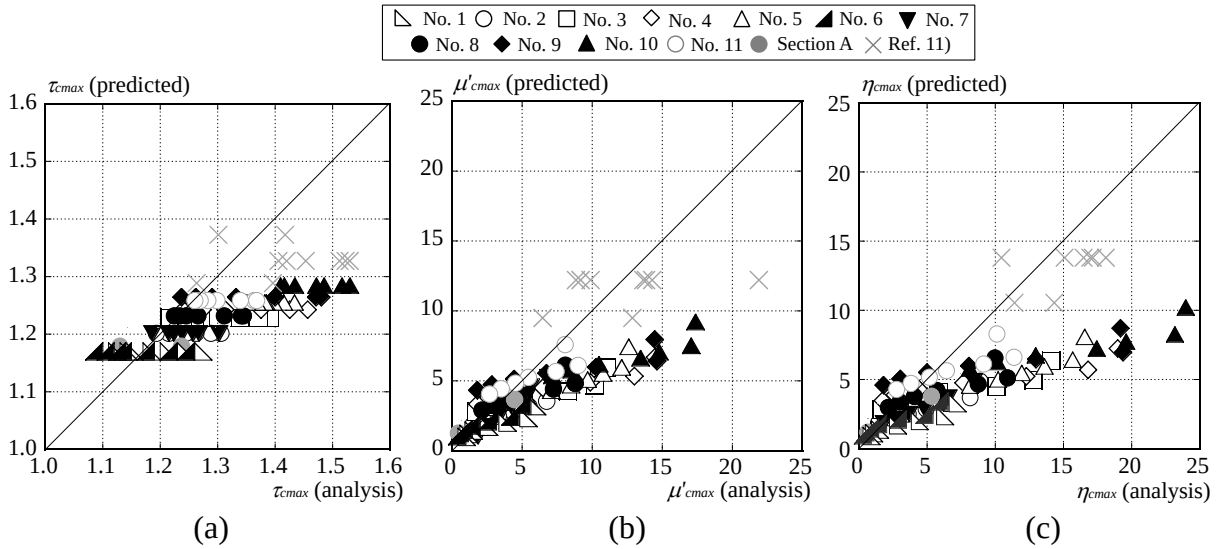
No. 1 No. 2 No. 3 No. 4 No. 5 No. 6 No. 7
No. 8 No. 9 No. 10 No. 11 Section A Ref. 11)
τcmax (predicted)
τcmax (analysis)
μ'cmax (predicted)
μ'cmax (analysis)
ηcmax (predicted)
ηcmax (analysis)
(a)
(b)
(c)

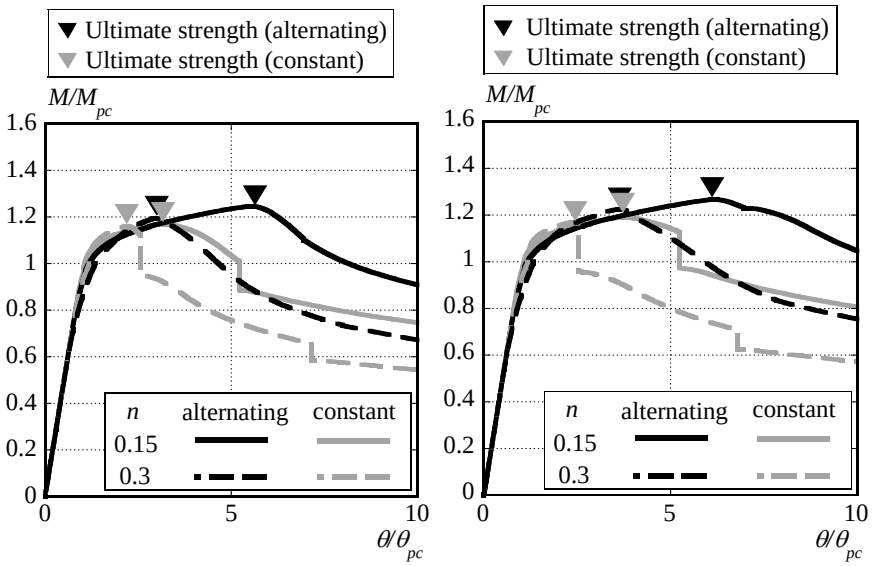
Ultimate strength (alternating)
Ultimate strength (constant)
M/M_pc
1.6
1.4
1.2
1
0.8
0.6
0.4
0.2
0
0
5
10
θ/θ_pc
n
alternating
constant
0.15
0.3
Ultimate strength (alternating)
Ultimate strength (constant)
M/M_pc
1.6
1.4
1.2
1
0.8
0.6
0.4
0.2
0
0
5
10
θ/θ_pc
n
alternating
constant
0.15
0.3

(a) (b)

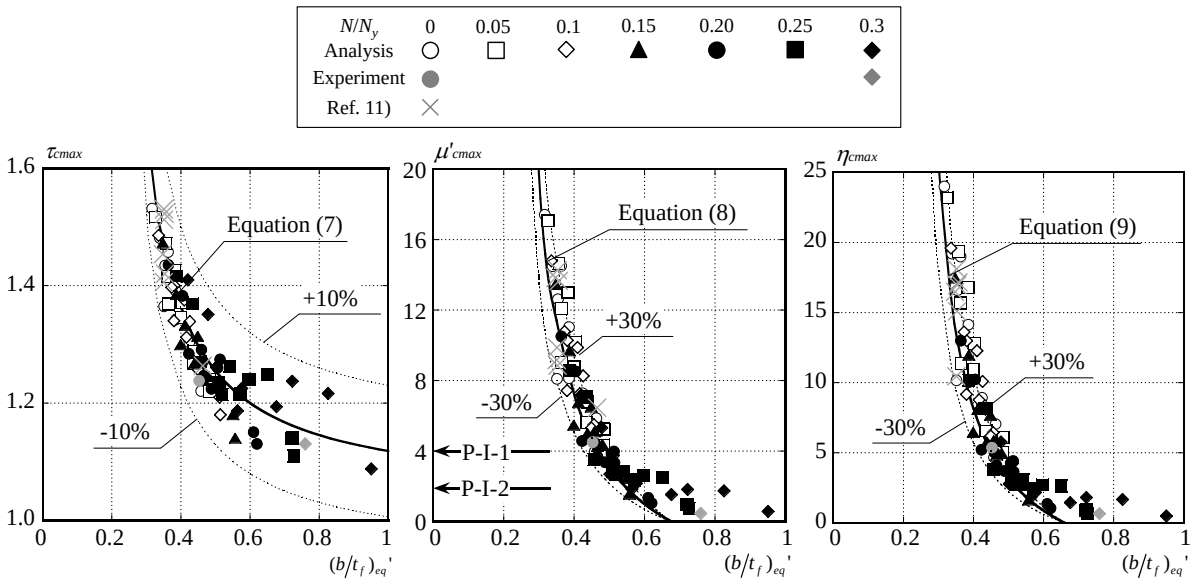
N/Ny
0
0.05
0.1
0.15
0.20
0.25
0.3
Analysis
Experiment
Ref. 11)
τcmax
Equation (7)
+10%
-10%
μ'cmax
Equation (8)
+30%
-30%
P-I-1
P-I-2
ηcmax
Equation (9)
+30%
-30%
(b/tf)eq'
(a)
(b)
(c)

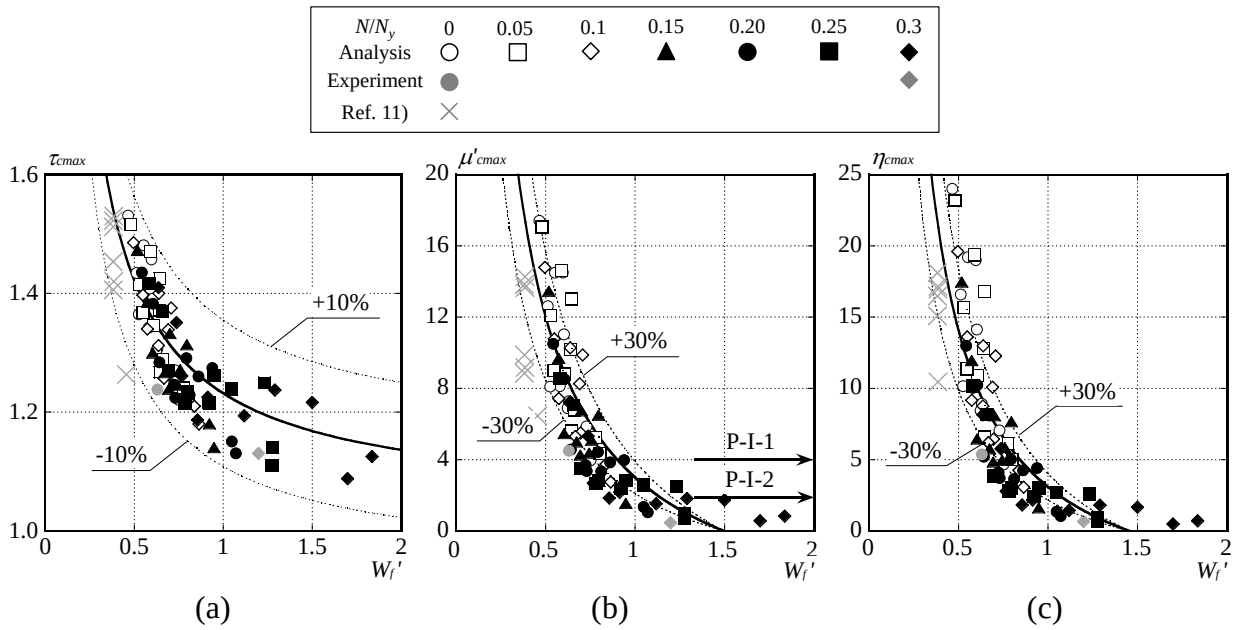
N/Ny
0
0.05
0.1
0.15
0.20
0.25
0.3
Analysis
Experiment
Ref. 11)
τcmax
+10%
-10%
μ'cmax
+30%
-30%
P-I-1
P-I-2
ηcmax
+30%
-30%
Wf'
Wf'
Wf'

(a) (b) (c)

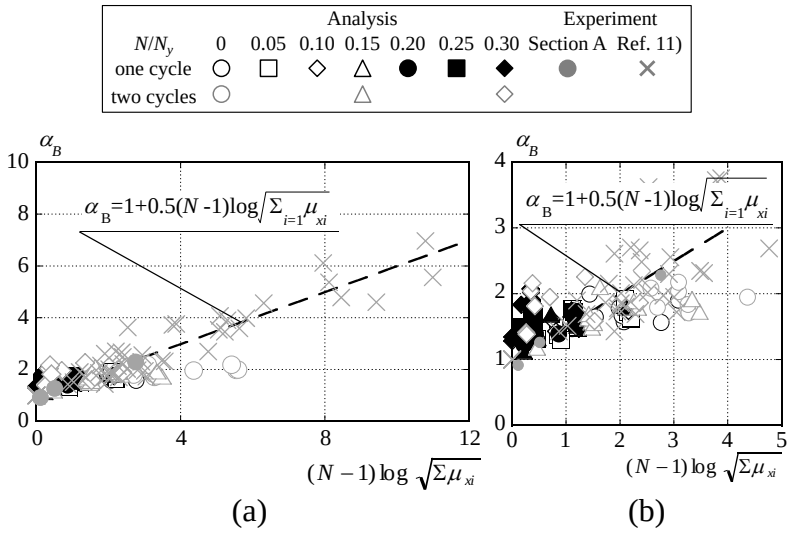
Analysis
Experiment
N/N_y
0
0.05
0.10
0.15
0.20
0.25
0.30
Section A
Ref. 11)
one cycle
two cycles
α_B
α_B=1+0.5(N -1)log√Σ_{i=1}μ_xi
(N −1) log √Σμ_xi
(a)
(b)

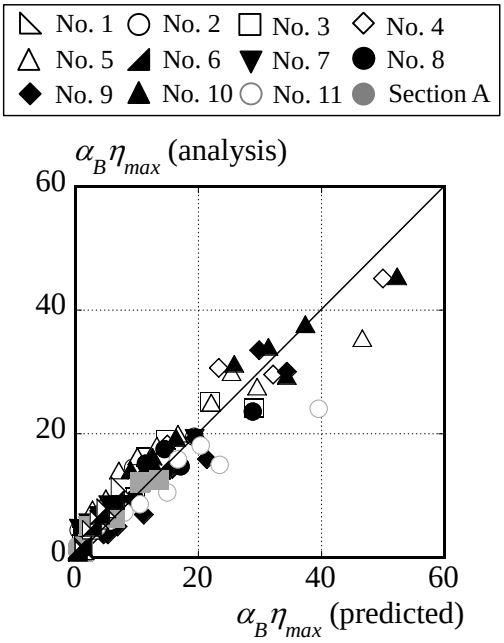
No. 1
No. 2
No. 3
No. 4
No. 5
No. 6
No. 7
No. 8
No. 9
No. 10
No. 11
Section A
$\alpha_B \eta_{max}$ (analysis)
60
40
20
0
0
20
40
60
$\alpha_B \eta_{max}$ (predicted)

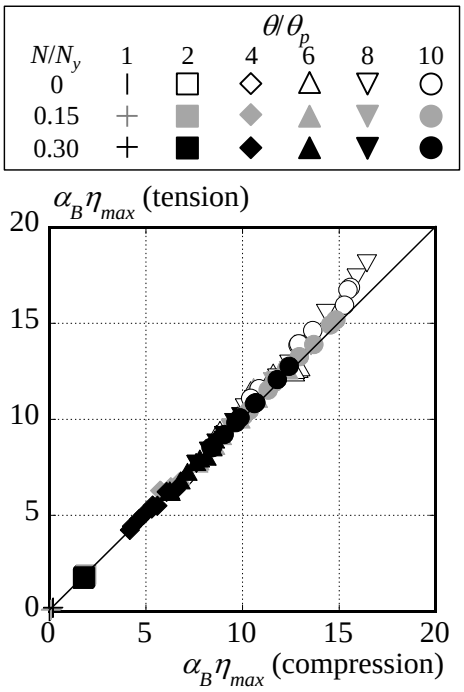
θ/θp
N/Ny
1
2
4
6
8
10
0
0.15
0.30
αBηmax (tension)
20
15
10
5
0
0
5
10
15
20
αBηmax (compression)

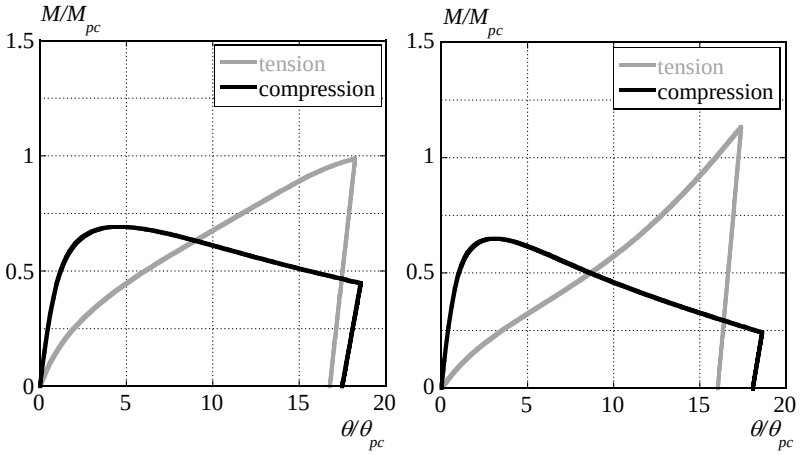
M/M_pc
1.5
1
0.5
0
0
5
10
15
20
θ/θ_pc
tension
compression
M/M_pc
1.5
1
0.5
0
0
5
10
15
20
θ/θ_pc
tension
compression

(a) (b)

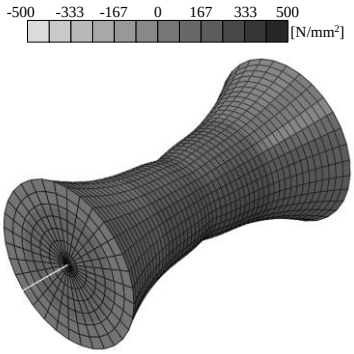
-500 -333 -167 0 167 333 500
[N/mm²]

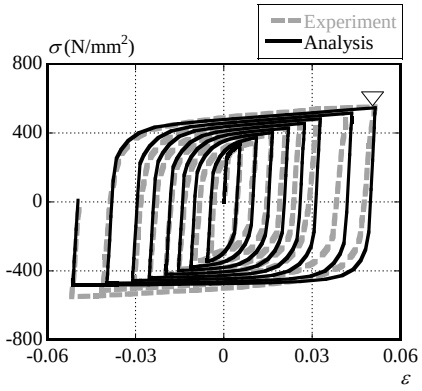
Experiment
Analysis
σ (N/mm2)
800
400
0
-400
-800
-0.06
-0.03
0
0.03
0.06
ε